Research paper

Photocatalytic hydrogen evolution over monolayer $H_{1.07}Ti_{1.73}O_4 \cdot H_2O$ nanosheets: Roles of metal defects and greatly enhanced performances

Yujie Song[a], Hao Wang[a], Jinhua Xiong[a], Binbin Guo[a,b], Shijing Liang[a,c,*], Ling Wu[a,b,*]

[a] *State Key Laboratory of Photocatalysis on Energy and Environment, Fuzhou University, Fuzhou, 350002, China*
[b] *Chinese Acad Sci, Fujian Inst Res Struct Matter, Fuzhou 350002, China*
[c] *Department of Environmental Science and Engineering, Fuzhou University, Fuzhou, 350108, China*

ARTICLE INFO

ABSTRACT

Monolayer $H_{1.07}Ti_{1.73}O_4 \cdot H_2O$ nanosheets with the thickness about 0.67 nm were prepared and developed as an efficient photocatalyst for hydrogen evolution. The prepared sample exhibits greatly improved photocatalytic activity with more 10.5 times higher than its layered counterpart. The morphologies, microstructures, superficial properties and electronic structures of the sample were characterized by XRD, TEM, AFM, BET, and UV–vis DRS in detail. Moreover, EXAFS, FTIR, XPS and in-suit FTIR of D_2O absorption results suggested that Ti vacancies result in the formation of abundant active O species around vacancies sites, which can be exposed fully in the monolayer nanosheets and bind with water molecules in the formation of surface coordination via hydrogen bonds. An efficient electron transition from nanosheets to surficial coordinated H_2O molecules takes place. Finally, a synergistic effect between titanium vacancies and ultrathin 2D structure was proposed to elucidate that the enhanced photocatalytic performance over metal defects may be attributed to efficient exposure of active species and transition of photo-electrons from surface to H_2O molecules.

1. Introduction

Hydrogen is a clean, green and environmental friendly energy. Photocatalytic water splitting to form hydrogen as a potential means for renewable energy production has attracted considerable attention [1,2]. Over the past decades, great efforts have been devoted to constructing and developing high efficient semiconductor photocatalysts for H_2 evolution. Various materials with special morphologies and structures, including mostly metal oxides, sulfides, and oxynitrides have been developed as potential photocatalysts for water splitting [3–6]. Among the reported nanomaterials, two-dimensional (2D) materials are particularly prominent and show encouraging performance in photocatalysis as well as other fields [7–12]. It has been studied that these 2D nanosheets can provide an extremely high percentage of exposed specific crystal facet, huge specific surface area, and large fraction of unsaturated surface metal sites due to their unique electronic structures and distinctive physicochemical properties [13–15]. Especially, the 2D materials with only monolayer thickness can greatly contribute to the separation and migration of photoelectron-hole pairs with recombination suppressed by reducing the travel distance of photo-generated electrons [13,16]. Therefore, there show enormous potentials of 2D materials to raise the opportunities of constructing new type

photocatalysts with high efficiency.

Until now, many ultrathin 2D materials including oxide nanosheets [17–19], MoS_2 nanosheet-based [20–22] and oxynitrides nanosheets [7–10,23–25] have been reported. Most of them are prepared from their layered structures via exfoliation process. In our previous studies, monolayer Ti-based and Nb-based nanosheets such as $H_2Ti_4O_9$, $H_2Ti_5O_{11}$ and HNb_3O_8 were developed and applied in photocatalytic water splitting [28–30]. It was revealed that these monolayer nanosheets show superior photocatalytic hydrogen evolution activities to their layered compounds. As for the photocatalytic hydrogen evolution, we hold that available active sites of catalysts for chemisorption and activation of water molecules are crucial in high efficient reaction systems. [31] But, what and how do they influence these available active sites? The influence of microstructures and electronic structures on the sites should be studied deeply. Because of the nontoxicity, high stability as well as inexpensive properties, [26] [27] special Ti-based nanosheets were selected and introduced in photocatalytic hydrogen evolution system for deeply exploring and understanding the effects of internal electron structures. Lepidocrocite titanates has an orthorhombic structure consisting of 2D corrugated layers of edge and corner sharing octahedral, such as $H_{2x}Ti_{2-x/2}\square_{x/2}O_4 \cdot H_2O$, $H_xTi_{2-x/4}\square_{x/4}O_4 \cdot H_2O$ and $H_xTi_{2-x/2}\square_{x/4}O_4 \cdot H_2O$. [32–35] These nonstoichiometric compounds

contain abundant Ti defects, which may produce many peculiar specificities. However, their physicochemical, electronic and optical properties have not been studied, not to mention their application researches. Therefore, it is a meaningful work to investigate the configuration characteristic and catalytic actions of lepidocrocite type structures.

Herein, we prepared lepidocrocite $H_{4x/3}Ti_{2-x/3}\square_{x/3}O_4 \cdot H_2O$ (x = 0.8, $\square$ = vacancy) nanosheets and developed these in photocatalytic system for H_2 evolution. Hydrogen evolution rate from water splitting over $H_{1.07}Ti_{1.73}O_4 \cdot H_2O$ nanosheets is up to 3.26 mmolh^{-1}g^{-1} under light irridations, which is over 10.5 times higher than that of the layered compound. The unique ultrathin structure, large specific surface area, available active sites, strong light response and improved photo-generated electrons migration efficiency on these monolayer nanosheets were investigated by TEM, AFM, BET and PL analysis. The influence of Ti vacancies on electron cloud density of surrounding oxygen atoms have been studied by XPS, FTIR and EXAFS. Based on in-suit FTIR of D_2O results, it is inferred that the exposed active oxygen atoms would balance their charges via hydrogen bonds with water molecules. Under light irradiation, chemisorbed water molecules are active and reduced by photoelectrons. Finally, a possible mechanism for the photocatalytic hydrogen evolution from water splitting over the monolayer nanosheets was proposed at a molecule level.

2. Material and method

2.1. Reagents and chemicals

Reagents such as anatase TiO_2, metal carbonates and tetra-butylammonium hydroxide (TBAOH) (40 wt% solution) used in this work were of analytical grade and without further purification. Deionized (DI) water (~18.2 MΩ cm) was used throughout the experiments.

2.2. Preparation of the $K_{0.8}Ti_{1.73}Li_{0.27}O_4$ and its protonic formation ($H_{1.07}Ti_{1.73}O_4 \cdot H_2O$)

The $K_{0.80}Ti_{1.73}Li_{0.27}O_4$ were prepared by a high temperature solid state reaction method. [36] Reagents such as TiO_2, K_2CO_3 and Li_2CO_3 were mixed uniformly with a molar ratio of 3:1:13. Then, the mixture was placed in a Pt crucible and reacted at 800 °C for 2 h. After cooling, the mixture was grinded into powder and then calcined at 1000 °C for 20 h, this process was repeated twice. Finally, the $K_{0.80}Ti_{1.73}Li_{0.27}O_4$ was achieved.

The obtained crystals were converted into a protonic form $H_{1.07}Ti_{1.73}O_4 \cdot H_2O$ by a method reported previously [36–38]. The $K_{0.80}Ti_{1.73}Li_{0.27}O_4$ were stirred in a 1 M HCl solution at ambient temperature for 24 h. The acid solution was replaced daily with a fresh for four times. Next, the precipitates were washed with enormous deionized water to remove acid residue. Finally, the products were dried at 60 °C in air.

2.3. Preparation of monolayer $H_{1.07}Ti_{1.73}O_4 \cdot H_2O$ nanosheets

The monolayer $H_{1.07}Ti_{1.73}O_4 \cdot H_2O$ nanosheets were obtained by a liquid exfoliation method [37,39] using tetrabutylammonium hydroxide solution $(C_4H_9)_4NOH$ (TBAOH) as intercalation agent. The procedure was as follows: 4.0 g layered $H_{1.07}Ti_{1.73}O_4 \cdot H_2O$ were immersed in 1000 mL diluted TBAOH aqueous solution with vigorously shaking for more than 4 days at the ambient temperature. Next, the obtained colloidal suspensions were treated with 1 M HCl solution, followed by washing with deionized water. Finally, the products were dried at 60 °Covernight, the monolayer $H_{1.07}Ti_{1.73}O_4 \cdot H_2O$ nanosheets were obtained which were measured by XRD.

2.4. Materials characterization

The X-ray diffraction (XRD) patterns were collected on a Bruker D8 Advance X-ray diffractometer with Cu Kα radiation (λ = 0.15406 nm). The amounts of K, Li and Ti in the products were measured by an inductively coupled plasma optical emission spectrometer (ICP-OES) (Ultima2, Jobin Yvon Co., France). The UV–vis diffuse reflectance spectra (UV-vis DRS) of the samples were obtained for the dry-pressed disk samples using a UV–vis spectrophotometer (Cary 500 Scan spectrophotometer, Varian). The Brunauer-Emmett-Teller (BET) specific surface area of the samples were measured by nitrogen adsorption/desorption isotherms at 77 K on an Autosorb-1C-TCD physical adsorption instrument (American Quantach-rome) using a Micrometrics ASAP 2020 system. Before analyzing, the samples were degassed in vacuum at 180 °C for 10 h. The transmission electron micrographs (TEM) were obtained by using a JEOL JEM-1010 electron microscope operating at an accelerating voltage of 200 kV. The scanning electron micrographs (SEM) were obtained by using a FEI Quanta 200F electron microscope. The photoluminescence (PL) spectra for samples were conducted on an Edinburgh FL/FS900 spectrophotometer. X-ray photoelectron spectroscopy (XPS) analysis was measured on a ESCALAB 250 photoelectron spectroscopy (Thermo Fisher Scientific Inc.) at 3.0 × 10–10 mbar with monochromatic Al Kα Radiation (E = 1486.2 eV). A tapping-mode atomic force microscope (AFM, Aglient 5500) with Si-tip cantilever was used to evaluate the morphology of the prepared nanosheets on the mica substrate.

2.5. In-situ FTIR measurement

The in-situ FTIR spectra of D_2O adsorbed on the samples were carried out on a Nicolet Nexus 670 Fourier transform infrared (FT-IR) spectrometer at a resolution of 4 cm^{-1}. A total of 64 scans were performed to acquire each spectrum. Firstly, the powder samples were first pressed into a self-supporting IR disk (18 mm diameter, 15 mg), then the disk was placed into the sample holder which could be moved vertically along the cell's tube by a magnet. Before initiating the FTIR measurements, the disk was treated under dynamic vacuum (6 × 10^{-4} Torr) at 150 °C for 3 h to remove surface contaminants. After the disk cooling to RT, 10 μL of D_2O was spiked into the cell with a syringe via the septum. 30 min later, after adsorption equilibrium was reached, the FTIR spectra of the samples were collected. The physisorbed D_2O was removed by a further evacuation at 150 °C for 3 min under 6 × 10^{-4} Torr, and then, another FTIR spectrum of the sample was then taken.

2.6. Electrochemistry measurement

The working electrode was prepared on fluorine-doped tin oxide (FTO) glass, which was cleaned by sonicating in chloroform, acetone and ethanol for 30 min. The glass was then rinsed with pure water (18 MΩ cm) and dried in air. The FTO slide was dip coated with 10 μL of slurry, which was obtained from mixture of 5 mg powder and 0.5 mL dimethylformamide with sonicating for 2 h. After air drying naturally, a copper wire was connected to the side part of the FTO glass using a conductive tape. The uncoated parts of the electrode were isolated with an epoxy resin and the exposed area of the electrode was 0.25 cm^2. The electrochemical measurements were performed in a conventional three electrode cell, using a Pt plate and a saturated Ag/AgCl electrode as counter electrode and reference electrode, respectively. The working electrode was immersed in a 0.2 M Na_2SO_4 aqueous solution without any additive for 20 s before measurement. The Mott–Schottky analysis and the electrochemical impedance spectroscopy (EIS) were performed at a Zahner electrochemical workstation. The photocurrent measurements were conducted on a Precision PARC workstation. A 300 W Xe lamp (Beijing Trustech, PLS-SXE300c) was used as a light source. Potentials were referenced to a reversible hydrogen electrode (NHE): E

(NHE) = E(Ag/AgCl) + (0.2 + 0.059 pH)V. The Mott-Schottky plots were obtained at three different frequencies (0.5 k, 1 k and 2 kHz).

2.7. H₂ evaluation of photocatalytic activity

The experiments of photocatalytic H_2 evolution were carried out in a glass enclosed gas circulation system fitted with a top Pyrex window. 80 mg of photocatalyst was dispersed in 80 mL aqueous solution containing 10% triethanolamine as sacrificial reagent. After degassing for 20 min, the suspension was irradiated with a Xe lamp (300 W), which is equipped with an IR cut filter ($\lambda \leq 800$ nm), to trigger the photocatalytic reaction. The photocatalytic reaction was conducted at 5 °C by a flow of cooling water. The generation of H_2 was analysed by a gas chromatography (Fuli GC9750) equipped with a TCD detector. The apparent quantum yield (AQY) is also measured under the photocatalytic reaction conditions of 350 nm. The incident light intensity of the Xe lamp is measured by Spectri Light ILT950. The total number of incident photons is measured using a calibrated silicon photodiode. The AQY is calculated according to the following equations:

$$\left\{ AQY(\%) = \frac{\text{The number of evolved hydrogen molecules} \times 2}{\text{The number of incident photon}} \times 100 \right\}$$

3. Results and discussion

XRD patterns and the 3D structures of as-prepared samples are shown in Fig. 1. It can be confirmed that the lepidocrocite-type $K_{0.80}Ti_{1.73}Li_{0.27}O_4$ is obtained with high crystalline. After a protonation process, the Li^+ cation and interlayer K^+ cation in $K_{0.80}Ti_{1.73}Li_{0.27}O_4$ can be fully extracted forming the layered $H_{1.07}Ti_{1.73}O_4·H_2O$ as the literature reported [37]. This can be proved by ICP-OES. The exchanged protons in the layered $H_{1.07}Ti_{1.73}O_4·H_2O$ are attached to interlayer H_2O molecules. Thus, most of the interlayer sites are occupied by H_3O^+ and remaining by H_2O [36]. It is found that the characteristic XRD peak of (020) shift to a lower angle from 11.47° for $K_{0.80}Ti_{1.73}Li_{0.27}O_4$ to 9.97° for layered $H_{1.07}Ti_{1.73}O_4·H_2O$. Correspondingly, the interlayer space expanded from 0.77 nm to 0.89 nm after the proton-exchange process according to the Bragg equation, which may be attributed to the larger ionic radius of H_3O^+ than K^+ [37]. The 3D structure of layered $H_{1.07}Ti_{1.73}O_4·H_2O$ shows that central Ti ion have adopted the six-coordinated, forming octahedral geometry. After the exfoliation process, the XRD pattern of the $H_{1.07}Ti_{1.73}O_4·H_2O$ nanosheets is too weak to be clearly observed, indicating the disappearing of the periodic layered structure of $H_{1.07}Ti_{1.73}O_4·H_2O$, which can be served as an evidence for the existence of $H_{1.07}Ti_{1.73}O_4·H_2O$ nanosheets.

The morphologies and structures of the obtained products were characterized by scanning electron microscopy (SEM) and transmission electron microscopy (TEM). Fig. 2 a shows a typical regular layered shape of $K_{0.80}Ti_{1.73}Li_{0.27}O_4$ and layered $H_{1.07}Ti_{1.73}O_4·H_2O$ (Fig. 2b), indicating that layered structure of $K_{0.80}Ti_{1.73}Li_{0.27}O_4$ is preserved during the protonation process. While the layered structure of
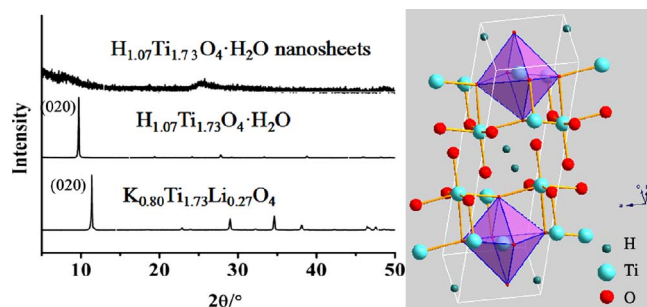

Fig. 1. Structures for the as-prepared samples (a) XRD pattern in comparison with the precursors, (b) 3D atomistic graph of the unit cell in ball-stick mode.

$H_{1.07}Ti_{1.73}O_4·H_2O$ is more loose than that of $K_{0.80}Ti_{1.73}Li_{0.27}O_4$ with the replacement of K^+ by H_3O^+, which may be attributed to the larger ionic radius of H_3O^+ than K^+. The $H_{1.07}Ti_{1.73}O_4·H_2O$ nanosheets were obtained from exfoliation of layered compounds (Fig. 2c). Moreover, interlayer distance of the layers can be also measured by the HRTEM image. Fig. 3 shows the HRTEM image of the layered $H_{1.07}Ti_{1.73}O_4·H_2O$. The lattice fringes of layers are obvious observed. Thus, the space value of lattice fringes can be considered as the interlayer distance of layers. According to the HRTEM image, the interlayer distance of layers is 0.87 nm, which is in good agreement with the calculated result (0.89 nm) based on the XRD data. TEM and SEAD images of the $H_{1.07}Ti_{1.73}O_4·H_2O$ nanosheets are shown in Fig. 4), the transparent feature and draped edges suggest that the prepared samples is ultrathin structure. Meanwhile, the thickness of the $H_{1.07}Ti_{1.73}O_4·H_2O$ nanosheets measured by AFM (Fig. 5) is only about 0.67 nm, which can be consider as the monolayer thickness.

Both Li^+ cations in the octahedron framework and interlayer K^+ cations in $K_{0.80}Ti_{1.73}Li_{0.27}O_4$ were extractable via the proton exchange process to form the layered $H_{1.07}Ti_{1.73}O_4·H_2O$ [35,38]. According to charge compensation scheme, every Li atom will be exchanged by one proton. Thus, there are two cases: (1) these protons are bonded to the oxygen atoms of the octahedra in which the Li ion was originally located forming the hydroxyl groups; (2) they are attached to the interlayer H_2O forming the H_3O^+ for the equilibrium charge. IR spectra may shed some light on them. [35,36] It have been reported that protonic titanates consisting protonic titanates consisting of −OH species in the octahedra will be exhibit absorption band at 950–1000 cm^{-1} because of bending mode of hydroxyls [35]. Therefore, the IR spectrum can be used to identify the statement of protons after the protons exchange process. Fig. 6a shows that the IR spectrum of $H_{1.07}Ti_{1.73}O_4·H_2O$ nanosheets have no signals at 950–1000 cm^{-1}, suggesting that the protons not bond to oxygen atoms of host frameworks that originally bond to Li atoms forming the hydroxyl groups. So, the leaching of Li ions may result in the metal vacancies in layered $H_{1.07}Ti_{1.73}O_4·H_2O$ and nanosheets (Fig. 6b).

After a proton exchange process, the Li^+ cations were leached from the octahedral sites (Ti/LiO_6) in $K_{0.80}Ti_{1.73}Li_{0.27}O_4$. However, these protons cannot occupy the octahedral sites originally located by the lattice Li atoms. Thus, amounts of defects may be left in the TiO_6 of $H_{1.07}Ti_{1.73}O_4·H_2O$. The defects would have great effect on the electronic structure of Ti and O atoms in the $H_{1.07}Ti_{1.73}O_4·H_2O$. Therefore, XPS was used to investigate the effect of the defects on the chemical states of surface atoms. The wide-scan XPS spectrum of the $K_{0.80}Ti_{1.73}Li_{0.27}O_4$ and $H_{1.07}Ti_{1.73}O_4·H_2O$ were showed in Fig. 7. The peaks of K and Li disappear after a protonation process, suggesting that K and Li atoms have been replaced by protons completely. Therefore, some interesting changes will be reflected on the Ti 2p and O 1s spectra. Thus, high resolution XPS spectra of Ti and O are further analysed in detail.

As shown in Fig. 8a. the symmetrical profiles is observed in the Ti 2p XPS spectrum of $K_{0.80}Ti_{1.73}Li_{0.27}O_4$, indicating that crystalline $K_{0.80}Ti_{1.73}Li_{0.27}O_4$ possess only a single oxidation state of the Ti atoms, the two Ti 2p Binding energy are 458.1($2p_{3/2}$) and 463.8($2p_{1/2}$) eV respectively (Table 1). We hold the opinion that Ti atoms in $K_{0.80}Ti_{1.73}Li_{0.27}O_4$ is tetravalent (Ti^{4+}) because $K_{0.80}Ti_{1.73}Li_{0.27}O_4$ is obtained through a high temperature and non-reduced environment. As for the $H_{1.07}Ti_{1.73}O_4·H_2O$ nanosheets, the Ti 2p XPS spectrum have a shift towards the high binding energy side, which may be resulted from the enhanced strength of Ti-O band from $K-O_1-Ti$ to $H-O_1-Ti$ during the protonation process. Ti $2p_{1/2}$ and Ti $2p_{3/2}$ can be fitted via introducing an additional component with a higher Binding energy. This new additional component can account for the enhanced Ti-O_1 band and the shift of Ti 2p in the $H_{1.07}Ti_{1.73}O_4·H_2O$ nanosheets. Because of the Ti vacancies sites, these O1 atoms will get electron from the TiO_6 octahedra nearby to keep balance [35]. The TiO_6 can be described as a distorted octahedron. The electronic structure of $H_{1.07}Ti_{1.73}O_4·H_2O$ nanosheets may be greatly changed.
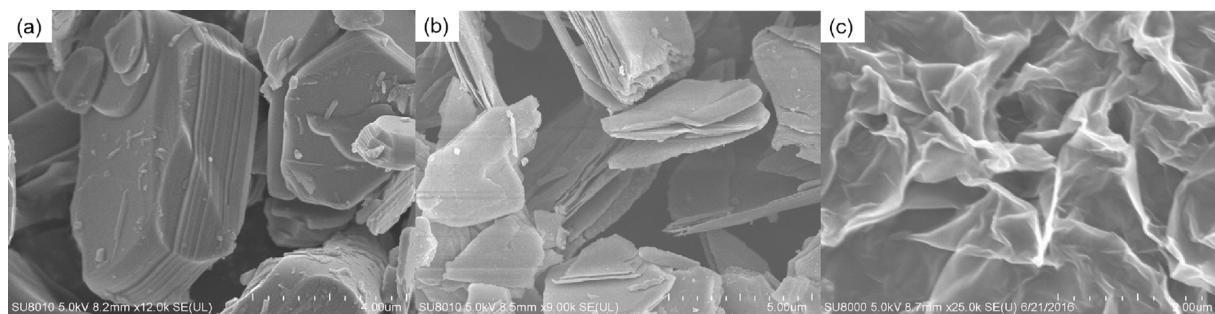
Fig. 2. SEM images of $K_{0.80}Ti_{1.73}Li_{0.27}O_4$ crystals (a), layered $H_{1.07}Ti_{1.73}O_4 \cdot H_2O$ (b), $H_{1.07}Ti_{1.73}O_4 \cdot H_2O$ nanosheets (c).
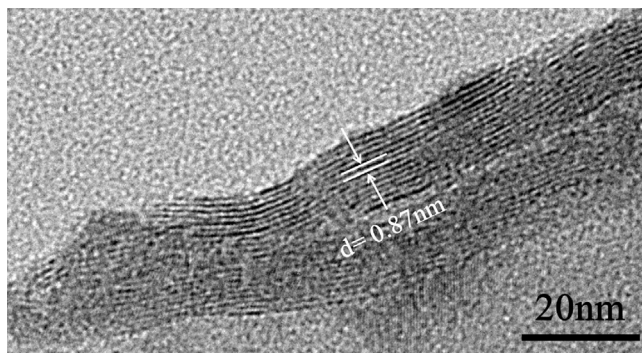

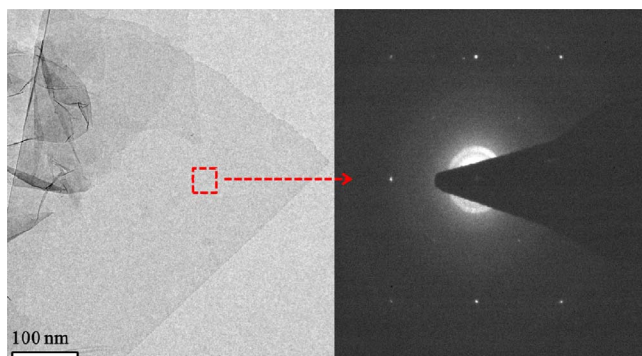**Fig. 3.** The HRTEM image of the layered $H_{1.07}Ti_{1.73}O_4 \cdot H_2O$.

Fig. 4. TEM images and selected area electron diffraction of $H_{1.07}Ti_{1.73}O_4 \cdot H_2O$ nanosheetss.
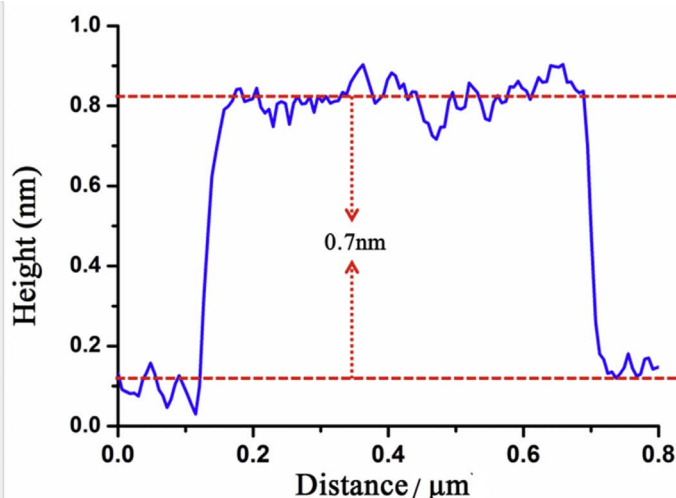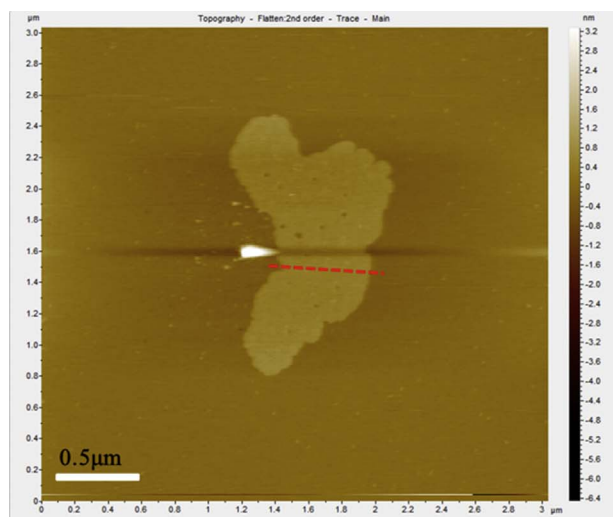
Meanwhile, the O1s spectra of $K_{0.80}Ti_{1.73}Li_{0.27}O_4$ and the $H_{1.07}Ti_{1.73}O_4 \cdot H_2O$ nanosheets have confirmed these results (Fig. 8b). Both of them can be de-convoluted into three peaks, which represent the 2-coordianted oxygen (O1), 4-coordianted oxygen (O2) and ad-sorbed oxygen species, respectively. The Binding energy of each peak is shown in Table 2. It can be seen that compared with $K_{0.80}Ti_{1.73}Li_{0.27}O_4$, the Binding energy of the O1 species in the $H_{1.07}Ti_{1.73}O_4 \cdot H_2O$ na-nosheets shows higher values, which may be attributed to weakened bond between the O1 species and the protons through hydrogen bonding [34]. According to Table 2, O2 species in the $K_{0.80}Ti_{1.73}Li_{0.27}O_4$ and the $H_{1.07}Ti_{1.73}O_4$ nanosheets have a similar Binding energy. These changed O1 species may be activated.

X-ray absorption near edge structure (XANES) and extended X-ray absorption fine structure (EXAFS) were used to investigate the co-ordination environments of Ti in $K_{0.80}Ti_{1.73}Li_{0.27}O_4$, layered $H_{1.07}Ti_{1.73}O_4 \cdot H_2O$ and nanosheets (Fig. 9). The XANES Ti K-edge os-cillation curve (Fig. 9a) for $H_{1.07}Ti_{1.73}O_4 \cdot H_2O$ nanosheets is similar with that for the layered $H_{1.07}Ti_{1.73}O_4 \cdot H_2O$, suggesting that the essential structures and the coordination environment around the Ti atoms maintained after the exfoliation process. However, the XANES Ti K-edge oscillation curve for $K_{0.80}Ti_{1.73}Li_{0.27}O_4$ is totally different from that for the $H_{1.07}Ti_{1.73}O_4 \cdot H_2O$. In addition, the enhanced signal for pre-edge in $K_{0.80}Ti_{1.73}Li_{0.27}O_4$ investigating that the coordination numbers and environments around Ti species have been greatly changed after proton-exchange process. Furthermore, The Fourier transform spectrum of the extended X-ray absorption structure (EXAFS) can further study the coordination environments around Ti atoms. In the K-space (Fig. 9b), the Ti K-edge XAFS $k^2\chi(k)$ oscillation curve for $H_{1.07}Ti_{1.73}O_4 \cdot H_2O$ nanosheets show the similar frequency with that for layered $H_{1.07}Ti_{1.73}O_4 \cdot H_2O$, but the amplitude for $H_{1.07}Ti_{1.73}O_4 \cdot H_2O$ nanosheets show the remarkable droop. These differences can be
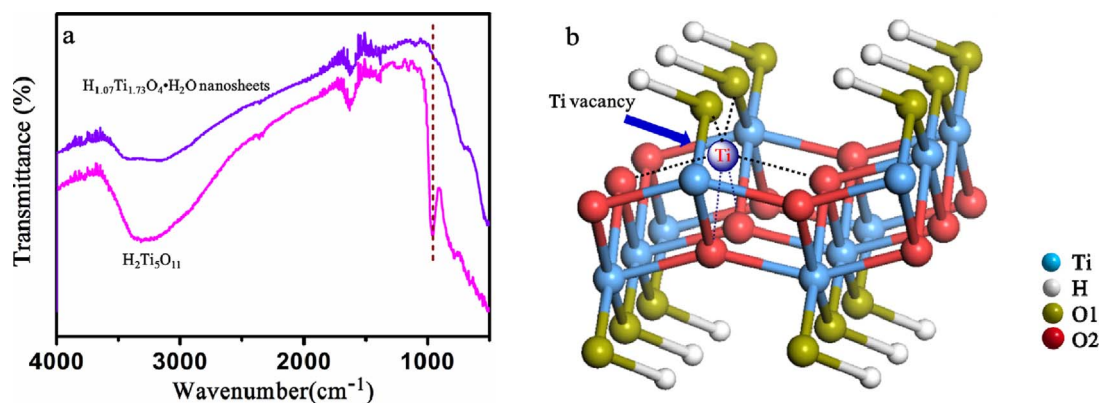

Fig. 5. AFM image of obtained $H_{1.07}Ti_{1.73}O_4 \cdot H_2O$ nanosheets.

Fig. 6. FT-IR spectra for $H_{1.07}Ti_{1.73}O_4 \cdot H_2O$ nanosheets and $H_2Ti_5O_{11}$ (a) and crystal structure of the monolayer $H_{1.07}Ti_{1.73}O_4 \cdot H_2O$ nanosheets (b).

further clearly manifested in R-space (the Fourier transform (FT) of K-space). As shown in Fig. 9c, two main peaks at 1.3 Å and 2.6 Å are observed in the FT curves for $H_{1.07}Ti_{1.73}O_4 \cdot H_2O$, associated with the Ti−O and Ti−Ti coordination, respectively. However, the peak positions of Ti−O and Ti−Ti coordinations in $K_{0.80}Ti_{1.73}Li_{0.27}O_4$ locate at 1.0 Å and 2.2 Å respectively. These results reveal that the bond length of the Ti-O and Ti-Ti are elongated slightly after the proton exchange resulting in the considerably increased disorder degree in structure. Moreover, the decreased intensity of Ti-O and Ti-Ti coordination in R-space suggest the decreased coordination numbers and concentrations of Ti atoms. Compared with the $K_{0.80}Ti_{1.73}Li_{0.27}O_4$, the $H_{1.07}Ti_{1.73}O_4 \cdot H_2O$ nanosheets possess the elongated Ti−O and Ti-Ti bonds as well as the higher disorder degree in structure. The significant disorder in $H_{1.07}Ti_{1.73}O_4 \cdot H_2O$ nanosheets could provide an open structure to efficiently expose the active sites [40–43].

Combining with the crystal structure of the nanosheets, the results of FTIR, XPS and XAFS indicate the existence of Ti defects in $H_{1.07}Ti_{1.73}O_4$ nanosheets. The Ti defects may be originated from the substitution of Li^+ cations and the proton exchange of the precursor $K_{0.80}Ti_{1.73}Li_{0.27}O_4$. The $K_{0.80}Ti_{1.73}Li_{0.27}O_4$ has an orthorhombic structure, which consist of two dimensional (2D) corrugated layers of edge and corner sharing TiO_6 octahedral. The K^+ cations locate in interlayer of two layers compensating for the negative charge that arises from the substitution of Li for Ti. It is noted that the alkali metal ions are exchangeable with a variety of inorganic and organic cations. Lattice Li^+ cations and the interlayer K^+ cations could be extracted after a proton exchange process. It is important that these hydrated protons can't occupy the sites of Li^+ cations in octahedral due to the large size of H_3O^+ [36], resulting in the vacancies of layered $H_{1.07}Ti_{1.73}O_4$ and $H_{1.07}Ti_{1.73}O_4$ nanosheets. Thus, these Ti vacancies would be retained and the sites of K^+ cations are replaced by H_3O^+ to keep the electric neutrality of the samples.

Morphological characteristics of samples should be studied for deeply understanding and exploring the advantages of the monolayer

naosheets. N_2 adsorption-desorption was measured to elucidate the difference of microstructure. As shown in Fig. 10, the BET surface area of the $H_{1.07}Ti_{1.73}O_4 \cdot H_2O$ nanosheets is as high as $176.3 m^2/g$, which is 20 times higher than that of the layered $H_{1.07}Ti_{1.73}O_4$ ($8.2 m^2/g$). Due to the very small interlayer distance of the adjacent layers, layered structure restrict the adsorption of N_2 molecules on the interlayer. The $H_{1.07}Ti_{1.73}O_4 \cdot H_2O$ nanosheets exfoliated from the parent LT has been overcome the steric inhibition of the adjacent layers. Thus, the measured surface area of the $H_{1.07}Ti_{1.73}O_4 \cdot H_2O$ nanosheets is much higher than that of layered $H_{1.07}Ti_{1.73}O_4$. Furthermore, the steric inhibition effect also limits the utilization of the active sites on the interlayer of layered $H_{1.07}Ti_{1.73}O_4$. The high amount of the exposed active sites could absorb more regent molecules to enhance the mass transfer. The photocatalytic activity would also be increased.

UV-vis diffuse reflectance (UV-vis DRS) spectra were employed to explore the optical properties of samples (Fig. 11). It is obvious that the layered $H_{1.07}Ti_{1.73}O_4 \cdot H_2O$ and $H_{1.07}Ti_{1.73}O_4 \cdot H_2O$ nanosheets have the similar spectral absorption but the absorption edge of $H_{1.07}Ti_{1.73}O_4 \cdot H_2O$ nanosheets appears an obvious blue shift ascribed to the quantum confinement effect of the monolayer structure. Meanwhile, the corresponding band gap can be calculated according to the Kubelk-Munk relation. The band gap energy of $H_{1.07}Ti_{1.73}O_4 \cdot H_2O$ nanosheets and layered precursor are about 3.4 eV and 3.25 eV respectively. Furthermore, the flat-band potential (V_{fb}) of this semiconductor was also measured by Mott-Schottky curves (Fig. 12). The V_{fb} of $H_{1.07}Ti_{1.73}O_4 \cdot H_2O$ nanosheets is about -0.88 V vs. NHE. It is generally known that the conduction band potentials (V_{CB}) of semiconductors are a little more negative (~ -0.1 V) than the flat band potential [44]. Thus, the V_{CB} of the $H_{1.07}Ti_{1.73}O_4 \cdot H_2O$ nanosheets is -0.98 V, which is more negative than the H_2O/H_2 potential (-0.41 V vs. NHE). Therefore, both of them are thermodynamically permissible for the photocatalytic hydrogen evolution by the photogenerated electrons.

Photocatalytic hydrogen production experiments were carried out over the as-prepared nanosheets. Fig. 13a shows the comparison of
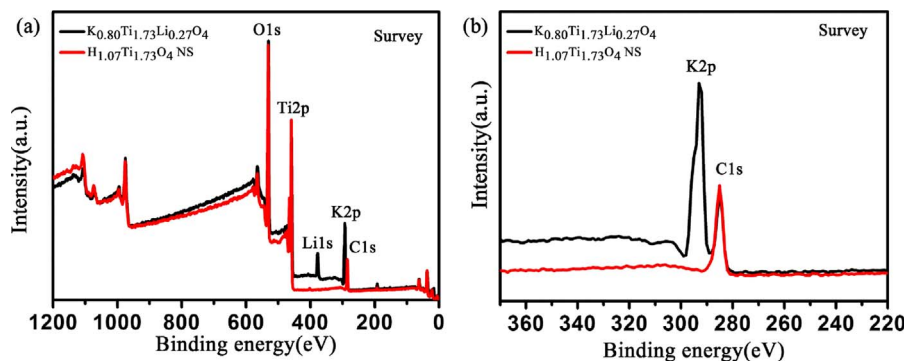

Fig. 7. Wide-scan XPS spectrum of $K_{0.80}Ti_{1.73}Li_{0.27}O_4$ and $H_{1.07}Ti_{1.73}O_4 \cdot H_2O$ nanosheets.
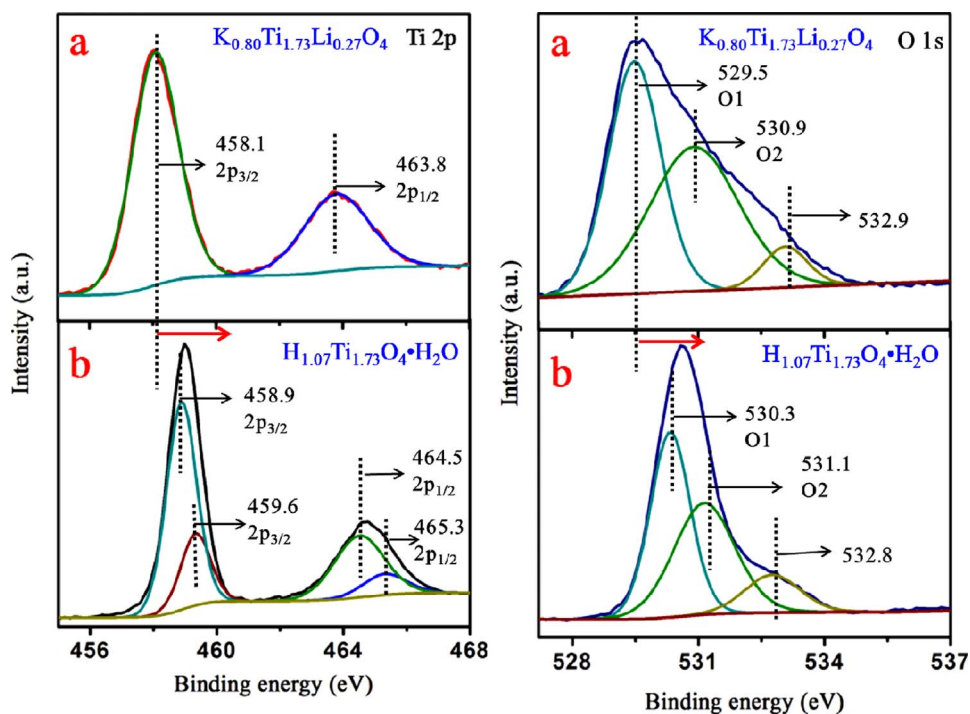
Table 1
Ti 2p Binding Energy and Energy Separation for $K_{0.80}Ti_{1.73}Li_{0.27}O_4$ and $H_{1.07}Ti_{1.73}O_4 \cdot H_2O$ (NS).

compounds	$2p_{3/2}$ (eV)	$2p_{1/2}$ (eV)	$\Delta 2p$ (eV)
$K_{0.80}Ti_{1.73}Li_{0.267}O_4$	458.1	463.8	5.7
$H_{1.07}Ti_{1.73}O_4 \cdot H_2O$ (NS)	458.9	464.5	5.6
	459.6	465.3	5.7

Table 2
O 1s Binding Energy and Energy Separation for $K_{0.80}Ti_{1.73}Li_{0.27}O_4$ and $H_{1.07}Ti_{1.73}O_4 \cdot H_2O$ (NS).

compounds	O1 (eV)	O2 (eV)	H_2O (eV)
$K_{0.80}Ti_{1.73}Li_{0.267}O_4$	529.5	530.9	532.9
$H_{1.07}Ti_{1.73}O_4 \cdot H_2O$ (NS)	530.3	531.1	532.8

Fig. 10. Nitrogen (N_2) adsorption-desorption isotherms of layered $H_{1.07}Ti_{1.73}O_4 \cdot H_2O$ and nanosheets.

hydrogen evolution over $H_{1.07}Ti_{1.73}O_4 \cdot H_2O$ nanosheets and layered samples. Compared with the poor photocatalytic hydrogen evolution rate of layered $H_{1.07}Ti_{1.73}O_4 \cdot H_2O$, the $H_{1.07}Ti_{1.73}O_4 \cdot H_2O$ nanosheets performed a higher photocatalytic activity. The hydrogen evolution rate was significantly enhanced to 3.26 mmol h^{-1} g^{-1}, which is more 10.5 times than that of the layered $H_{1.07}Ti_{1.73}O_4 \cdot H_2O$
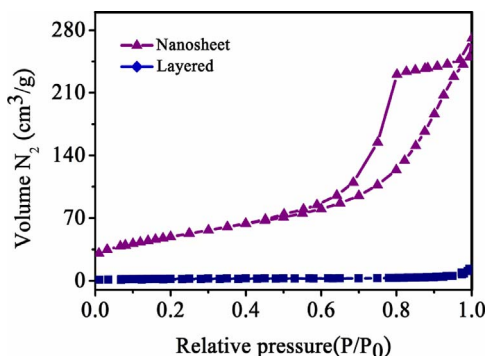
(0.31 mmol h^{-1} g^{-1}). After the 6 h, the amount of the hydrogen evolution is up to 19.1 mmol g^{-1} over the nanosheets 10.2 times higher than that of the layered compart (1.88 mmol g^{-1}). Moreover, the hydrogen evolution rate of the $H_{1.07}Ti_{1.73}O_4 \cdot H_2O$ nanosheets is 6 times higher than that of the anatase TiO_2. Furthermore, the photocatalytic activity of the $H_{1.07}Ti_{1.73}O_4$ nanosheets was further evaluated by irradiating at 350 nm to calculate the AQY. The AQY of $H_{1.07}Ti_{1.73}O_4$
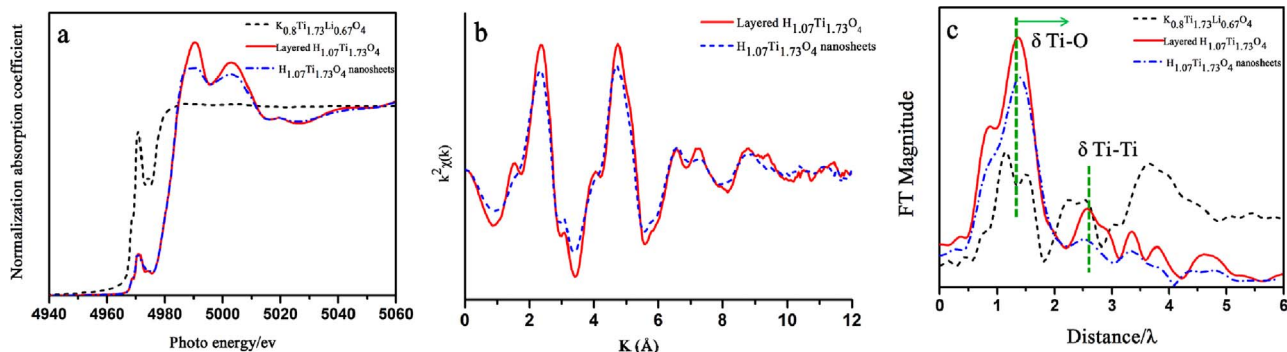

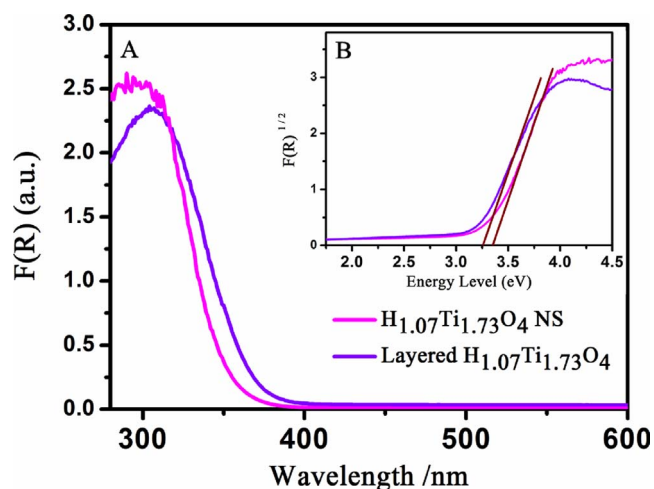Fig. 9. Ti K-edge XANES (a) and EXAFS (b) spectra for as-prepared samples.

Fig. 11. (A) UV-vis diffuse reflectance spectrometry of layered $H_{1.07}Ti_{1.73}O_4 \cdot H_2O$ and nanosheets. (B) (Fhυ)$^{0.5}$ as a function of photonenergy (hυ), where F is the Kubelka–Munk function.

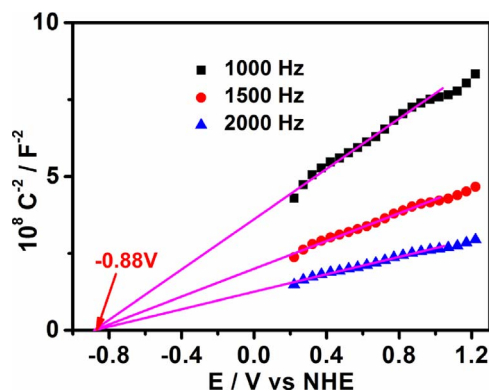**Fig. 12.** Mott-Schottky plots of the monolayer $H_{1.07}Ti_{1.73}O_4 \cdot H_2O$ nanosheets.

nanosheets is about 46.4%, which is 10.5 and 5.9 times higher than that over layered $H_{1.07}Ti_{1.73}O_4$ (4.42%) and anatase TiO_2 (7.69%), respectively. Moreover, $H_{1.07}Ti_{1.73}O_4 \cdot H_2O$ nanosheets showed high active stability of hydrogen evolution. As Fig. 13b shows, a prolonged photocatalytic reaction in 16 h, while no obvious loss of the photocatalytic activity is observed over $H_{1.07}Ti_{1.73}O_4$ nanosheets. Furthermore, the source of hydrogen was detected by D_2O. Under the same conditions, D_2 was detected suggesting that the obtained monolayer nanosheets can photocatalytic hydrogen generation from water splitting.

The photocatalytic process of H_2O molecules over the prepared sample should be studied thoroughly. Titanium vacancies have been considered as surface active sites for water adsorption and water splitting [45]. Because of the Ti defect sites and distorted TiO_6

octahedral geometry structure of the prepared nanosheets, the active O species surrounding Ti atoms may greatly promote the activation and reduction of H_2O. If these active O species could be exposed, the efficiency of photocatalysis can be further enhanced. In-suit FTIR of D_2O adsorption was carried out to confirm this point. Fig. 14(A) shows that the D_2O molecules can chemisorb on the surface of $H_{1.07}Ti_{1.73}O_4 \cdot H_2O$ nanosheets even with evacuation at 150 °C. The strong peaks are located at 1206 and 2885 cm^{-1} can attribute to the ν_{D-O} and δ_{D-O} vibration peaks respectively, which have a red shift to D_2O at 2750 cm^{-1} [46,47]. These results revealed that H_2O molecules can be chemisorbed at the surface of nanosheets with Ti−O⋯H−O−H coordination. The activate H_2O molecules would be easily reduced by photogenerated electrons to produce H_2 under the light irradiation. In contrast, these peaks on layered compound are much weaker (Fig. 14B) suggesting that the monolayer structure can dramatically increase the amount of exposed active sites. Therefore, the synergistic effect form between Ti defect sites and the monolayer structure in photocatalysis, which greatly enhances catalytic activities by promoting the exposer of actives and migration of interfacial charge from the excited defect of surface to H_2O.

As aforementioned, electrochemical analysis and photoluminescence spectra (PL) were carried out to confirm the transformation and separation of photogenerated carrier course. Transient photocurrent responses (Fig. 15A) reveal that the interfacial electron transfer over $H_{1.07}Ti_{1.73}O_4 \cdot H_2O$ nanosheets is more favourable suggesting the high transformation and separation efficiency of the photogenerated electrons-holes compared with the layered structure. These results can be also proved by electrochemical impedance spectroscopy (EIS) (Fig. 15B). Nyquist impedance of $H_{1.07}Ti_{1.73}O_4 \cdot H_2O$ nanosheets has the smaller arc followed by layered $H_{1.07}Ti_{1.73}O_4 \cdot H_2O$ which has a bigger arc compared with the former, suggesting that the transformation of photogenerated electrons from interior to interface are easier over nanosheets. The PL spectra were used to measure the separation rate of electron-hole pairs. (Fig. 16). It is clearly seen that the $H_{1.07}Ti_{1.73}O_4$ nanosheets exhibit much weaker photoluminescence intensity than that of the layered $H_{1.07}Ti_{1.73}O_4$, indicating that initial charges have more possibilities transferred to surface of catalysts and further to the bound H_2O molecules. Thus, the charge separation of the samples would be greatly promoted after exfoliating the layered structure into the nanosheets, enhancing the photocatalytic activities of the samples. Moreover, more active atoms can be efficiently exposed in the nanosheets by removing the steric effect in the layered structure after the exfoliation process. These active atoms play the indispensable roles in the adsorption and activation of reactant molecules, and further promoting the surface charge transfer from photocatalyst to reactant molecules. It is the synergistic effect between the ultrathin 2D structure and surface defects (titanium vacancies) that results in the efficient photocatalytic activity for water splitting.

Based on experimental results, a probable mechanism for photocatalytic hydrogen evolution over the monolayer $H_{1.07}Ti_{1.73}O_4 \cdot H_2O$ nanosheets was proposed. Water molecules can be chemisorbed and
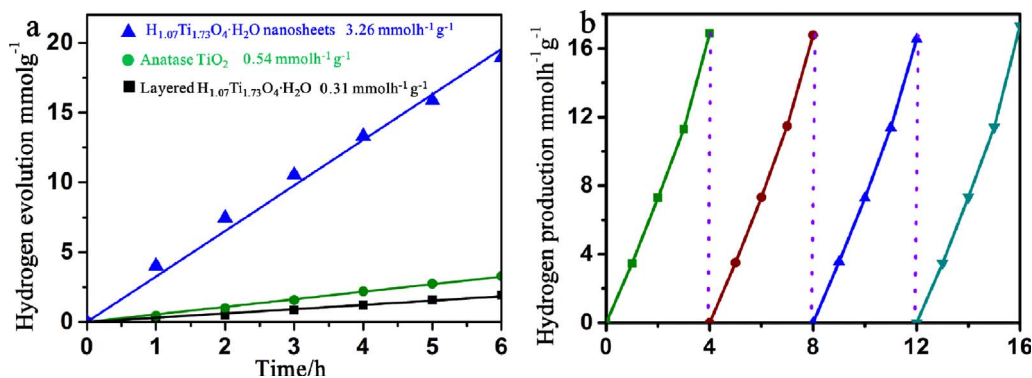

Fig. 13. (a) Hydrogen evolution of layered $H_{1.07}Ti_{1.73}O_4$ and $H_{1.07}Ti_{1.73}O_4 \cdot H_2O$ nanosheets. (b). Hydrogen evolution of $H_{1.07}Ti_{1.73}O_4$ nanosheets for 16 h.
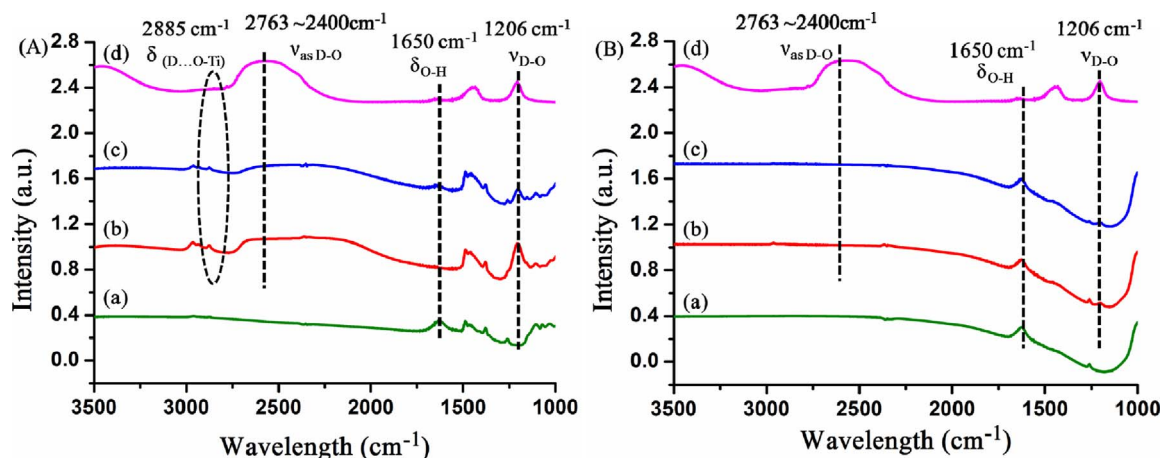
Fig. 14. In situ FTIR spectra of the $H_{1.07}Ti_{1.73}O_4$ nanosheets (A) and layered compound (B) for D_2O-adsorbed. (a) After degassing at 150 °C for 4 h. (b) Adsorption for 30 min at RT (physisorption + chemisorption). (c) Further evacuation of excess probe molecules at 150 °C for 5 min (chemisorption). (d) FTIR spectra of D_2O.

activated on the exposed surface active O species around Ti defect sites (Scheme 1). Since the higher conduction band position of $H_{1.07}Ti_{1.73}O_4 \cdot H_2O$ nanosheets than H_2O/H_2, a directional transfer of the photogenerated electrons from catalyst to H_2O is feasible and dynamic permission. Under simulated solar irradiation, the internal photo-electrons will transfer a short distance to the surface of the $H_{1.07}Ti_{1.73}O_4 \cdot H_2O$ nanosheets and perform a strong redox potential to reduce H^+ to H_2, while the holes would be consumed by TEOA (Scheme 2). The synergistic effect between Ti vacancies and the monolayer 2D structure meshed perfectly to promote separation of initial charge and inhibit electrons-holes recombination as well as promote the interfacial charge transfer from the excited defects to H_2O. Then, the efficient photocatalytic hydrogen evolution from water splitting achieved.

4. Conclusions

In summary, we have introduced the monolayer protonic titanate nanosheets ($H_{1.07}Ti_{1.73}O_4 \cdot H_2O$) with the thickness of about 0.7 nm as an efficient photocatalyst for hydrogen evolution from water splitting. The photocatalytic hydrogen evolution rate over the monolayer nanosheets are more 10.5 times than that of the layered compound. XRD, XPS, TEM, AFM, FTIR and BET analysis clearly reveals the microstructures and micromorphologies of the as-prepared nanosheets. EXAFS and XPS analysis suggest that abundant defects of Ti vacancies were formed after a proton exchange process. In addition, Ti coordination environment, the electron cloud density of the surrounded O atoms and distorted octahedral geometry are greatly changed after the exfoliation process, which results in the formation and exposures of active O species. In-suit FTIR of D_2O absorption reveals that these exposed active sites can greatly contribute to the activation of water molecules via the formation of surficial complexes by hydrogen bonds. The Ti vacancies may act as the initial charge carriers' acceptor to transfer the photo-
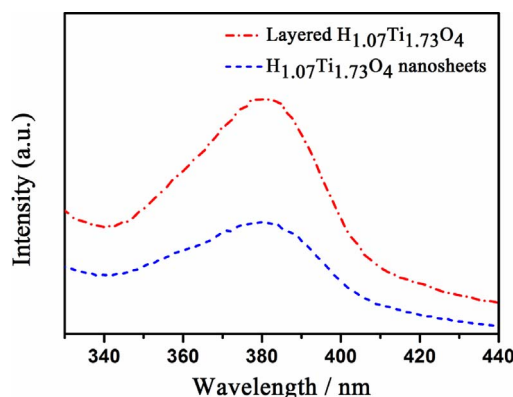

Fig. 16. Photoluminescence spectra of layered $H_{1.07}Ti_{1.73}O_4 \cdot H_2O$ and nanosheet.

generated electrons from the photocatalyst to absorbed water molecules. Based on mentioned experimental results, a synergistic effect between Ti defect sites and the monolayer structure was supposed, which greatly enhanced the charge transfer rate and efficiency separation of electron-hole pairs. Moreover, the heterogeneous catalyst can keep initial catalytic efficiency even after four times reused. We believe that the present study of monolayer thickness compound with abundant vacancies will stimulate intensive exploration in the construction and design of high efficient photocatalysts for green and universal photocatalysis applications.
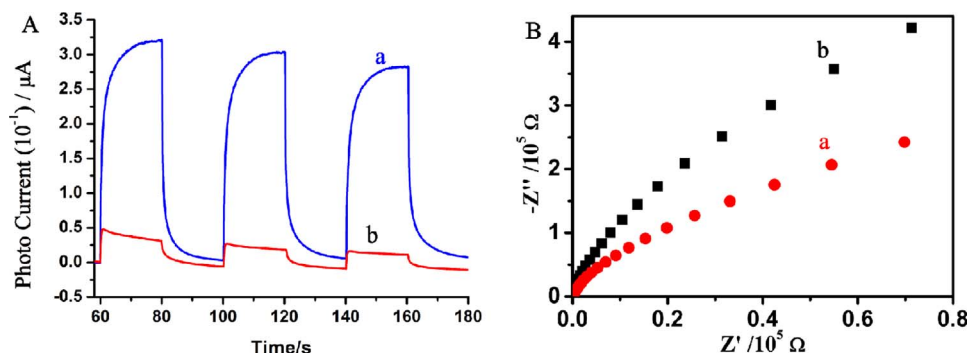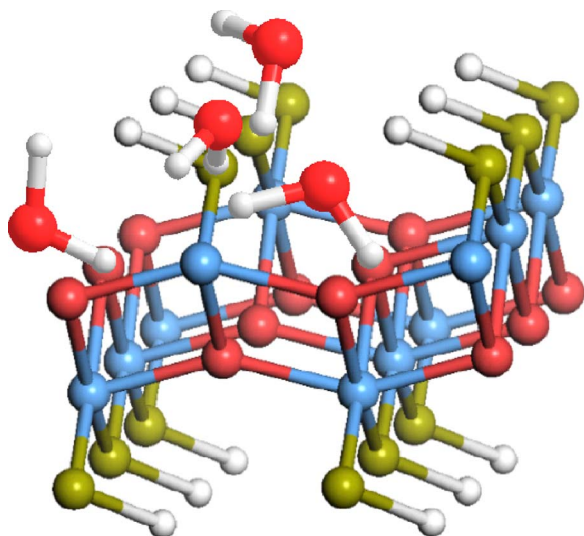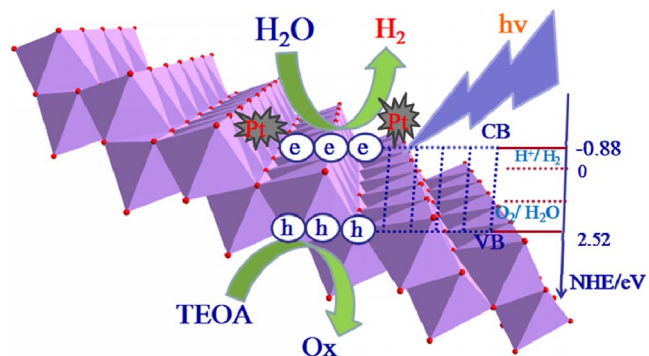
Acknowledgements

Fig. 15. Transient photocurrent response of $H_{1.07}Ti_{1.73}O_4 \cdot H_2O$ nanosheets (a) and layered $H_{1.07}Ti_{1.73}O_4 \cdot H_2O$ (b). (B) Nyquist impedance plots of $H_{1.07}Ti_{1.73}O_4 \cdot H_2O$ nanosheets (a) and layered $H_{1.07}Ti_{1.73}O_4 \cdot H_2O$ (b).

Scheme 1. Water molecules are chemisorbed in the monolayer nanosheets.

Scheme 2. Mechanism diagram of $H_{1.07}Ti_{1.73}O_4 \cdot H_2O$ nanosheets for hydrogen evolution.

References

[1] K. Maeda, K. Domen, J. Phys. Chem. Lett. 1 (2010) 2655–2661.
[2] T. Hisatomi, J. Kubota, K. Domen, Chem. Soc. Rev. 43 (2014) 7520–7535.
[3] A. Kudo, Y. Miseki, Chem. Soc. Rev. 38 (2009) 253–278.
[4] H. Pan, Renew. Sustain. Energy Rev. 57 (2016) 584–601.
[5] M. Ni, M.K.H. Leung, D.Y.C. Leung, K. Sumathy, Renew. Sustain. Energy Rev. 11 (2007) 401–425.
[6] R. Abe, M. Higashi, K. Domen, J. Am. Chem. Soc. 34 (2010) 11828–11829.
[7] R.M. Navarro Yerga, M.C. Alvarez Galvan, F. del Valle, J.A. Villoria de la Mano, J.L. Fierro, ChemSusChem 2 (2009) 471–485.
[8] C. Xue, H. An, X. Yan, J. Li, B. Yang, J. Wei, G. Yang, Nano Energy 39 (2017) 513–523.
[9] B. Lin, G. Yang, B. Yang, Y. Zhao, Appl. Catal. B: Environ. 198 (2016) 276–285.
[10] B. Lin, H. An, X. Yan, T. Zhang, J. Wei, G. Yang, Appl. Catal. B: Environ. 210 (2017) 173–183.
[11] F.E. Osterloh, Chem. Soc. Rev. 42 (2013) 2294–2320.
[12] F.E. Osterloh, B.A. Parkinson, MRS Bull. 36 (2011) 17–22.
[13] S. Ida, T. Ishihara, J. Phys. Chem. Lett. 5 (2014) 2533–2542.
[14] Y. Ebina, T. Sasaki, M. Harada, M. Watanabe, Chem. Mater. 14 (2002) 4390–4395.
[15] S. Liang, L. Wen, S. Lin, J. Bi, P. Feng, X. Fu, L. Wu, Angew. Chem. 53 (2014) 2951–2955.
[16] J. Xiong, L. Wen, F. Jiang, Y. Liu, S. Liang, L. Wu, J. Mater. Chem. A 3 (2015) 20627–20632.
[17] S. Ida, Y. Okamoto, M. Matsuka, H. Hagiwara, T. Ishihara, J. Am. Chem. Soc. 134 (2012) 15773–15782.
[18] Y. Okamoto, S. Ida, J. Hyodo, H. Hagiwara, T. Ishihara, J. Am. Chem. Soc. 133 (2011) 18034–18037.
[19] S. Ida, Y. Okamoto, S. Koga, H. Hagiwara, T. Ishihara, RSC Adv. 3 (2013) 11521.
[20] J.-K. Lee, W. Lee, T.-J. Yoon, G.-S. Park, J.-H. Choy, J. Mater. Chem. 12 (2002) 614–618.
[21] F.A. Frame, F.E. Osterloh, J. Phys. Chem. C 114 (2010) 10628–10633.
[22] Y. Li, H. Wang, L. Xie, Y. Liang, G. Hong, H. Dai, J. Am. Chem. Soc. 133 (2011) 7296–7299.
[23] K. Maeda, M. Higashi, D. Lu, R. Abe, K. Domen, J. Am. Chem. Soc. 132 (2010) 2655–2661.
[24] M. Higashi, K. Domen, R. Abe, J. Am. Chem. Soc. 134 (2012) 6968–6971.
[25] K. Maeda, K. Domen, MRS Bull. 36 (2011) 25–31.
[26] Y. Chen, J.C. Crittenden, S. Hackney, L. Sutter, D.W. Hand, Environ. Sci. Technol. 39 (2005) 1201–1208.
[27] I.N. Martyanov, S. Uma, S. Rodrigues, K.J. Klabunde, Chem. Commun. 21 (2004) 2476–2477.
[28] S. Sun, D. Yang, G. Zhang, E. Sacher, J.P. Dodelet, Chem. Mater. 19 (2007) 6376–6378.
[29] J. Xiong, Y. Liu, C. Cao, L. Shen, W. Wu, S. Liang, R. Liang, L. Wu, J. Mater. Chem. A 3 (2015) 6935–6942.
[30] Q. Xiang, J. Yu, M. Jaroniec, J. Am. Chem. Soc. 134 (2012) 6575–6578.
[31] M.M. Haque, M. Khan, K. Umar, N.A. Mir, M. Muneer, T. Harada, M. Matsumura, Energy Environ. Focus 2 (2013) 73–78.
[32] M.K. Nowotny, L.R. Sheppard, T. Bak, J. Nowotny, J. Phys. Chem. C 112 (2008) 5275–5300.
[33] Y.K. Jo, I.Y. Kim, J.L. Gunjakar, J.M. Lee, N.S. Lee, S.H. Lee, S.J. Hwang, Chem. Eur. J. 20 (2014) 10011–10019.
[34] T. Gao, H. Fjellvåg, P. Norby, Inorg. Chem. 48 (2009) 1423–1432.
[35] T. Gao, H. Fjellvåg, P. Norby, Chem. Mater. 21 (2009) 3503–3513.
[36] T. Sasaki, F. Kooli, M. Iida, Y. Michiue, S. Takenouchi, Y. Yajima, Fujio Izumi, B.C. Chakoumakos, M. Watanabe, Chem. Mater. 10 (1998) 4123–4128.
[37] T. Sasaki, M. Watanabe, J. Am. Chem. Soc. 120 (1998) 4682–4689.
[38] T. Tanaka, Y. Ebina, K. Takada, K. Kurashima, T. Sasaki, Chem. Mater. 15 (2003) 3564–3568.
[39] T. Maluangnont, K. Matsuba, F. Geng, R. Ma, Y. Yamauchi, T. Sasaki, Chem. Mater. 25 (2013) 3137–3146.
[40] Y. Sun, Z. Sun, S. Gao, H. Cheng, Q. Liu, F. Lei, S. Wei, Y. Xie, Adv. Energy Mater. 4 (2014) 1300611.
[41] Y.F. Zhao, G.B. Chen, T. Bian, C. Zhou, G.I.N. Waterhouse, L.Z. Wu, C.H. Tung, L.J. Smith, D. O'Hare, T.R. Zhang, Adv. Mater. 27 (2015) 7824–7831.
[42] S. Gao, Z.T. Sun, W. Liu, X.C. Jiao, X.L. Zu, Q.T. Hu, Y.F. Sun, T. Yao, W.H. Zhang, S.Q. Wei, Y. Xie, Nat. Commun. 8 (2017) 14503.
[43] F. Farges, Phys. Rev. B 56 (1997) 1809–1819.
[44] Y. Shao, C. Cao, S. Chen, M. He, J. Fang, J. Chen, X. Li, D. Li, Appl. Catal. B: Environ. 179 (2015) 344–351.
[45] J. Nowotny, M.A. Alim, T. Bak, M.A. Idris, M. Ionescu, K. Prince, M.Z. Sahdan, K. Sopian, M.A. Mat Teridi, W. Sigmund, Chem. Soc. Rev. 44 (2015) 8424–8442.
[46] K. Hadjiivanov, H. Knözinger, B. Tsyntsarski, L. Dimitrov, Catal. Lett. 62 (1999) 35–40.
[47] P. Gupta, A.C. Dillon, A.S. Bracker, S.M. George, Surf. Sci. 245 (1991) 360–372.